Near infrared to ultraviolet optical properties of bulk single crystal and nanocrystal thin film iron pyrite

Near infrared to ultraviolet optical properties of bulk single crystal and nanocrystal thin film iron pyrite

Indra Subedi, Khagendra P Bhandari, Randall J Ellingson and Nikolas J Podraza

Department of Physics and Astronomy & Wright Center for Photovoltaics Innovation and Commercialization, University of Toledo, Toledo, OH 43606, USA

E-mail: nikolas.podraza@utoledo.edu

CrossMark

Abstract

We report optical properties of iron pyrite (FeS_2) determined from *ex situ* spectroscopic ellipsometry measurements made on both a commercially available bulk single crystal and nanocrystalline thin film over a spectral range of 0.735–5.887 eV. The complex dielectric function, $\varepsilon(E) = \varepsilon_1(E) + i\varepsilon_2(E)$, spectra have been determined by fitting a layered parametric model to the ellipsometric measurements. Spectra in ε are modeled using a Kramers–Kronig consistent critical point parabolic band model involving seven critical points for the bulk single crystal and four critical points for the nanocrystalline film. Absorption coefficient spectra for both types of samples are also determined from ε. Critical point features in the nanocrystalline films are broader, have lower amplitude and lower energy critical points detected having a small blue shift when compared to the single crystal sample.

(Some figures may appear in colour only in the online journal)

1. Introduction

Iron pyrite (FeS_2) is an important source of iron and sulfur and is the most abundant, non-toxic, naturally occurring sulfur mineral found in the Earth's crust. The iron pyrite crystal structure consists of a face centered cubic lattice [1], where each iron atom is octahedrally coordinated by six sulfur atoms and each sulfur atom is tetrahedrally coordinated with one neighboring sulfur atom and three neighboring iron atoms [2, 3]. Due to having a high optical absorption coefficient (α) in the near infrared and visible regions, band gap energy near ~1 eV, and low material cost, thin film FeS_2 has been considered an appealing potential absorber layer in thin film photovoltaics (PV) applications [4–9]. Despite these promising properties, no efficiency improvements in working PV devices based on FeS_2 absorbers have been demonstrated since 1993 when Ennaoui *et al* reported 2.8% efficient devices [5]. In recent years, attention has been focused on solution based synthesis of FeS_2 nanocrystals as a low-temperature route to inexpensive solar cells [8, 9]. Although advances in PV based on FeS_2 absorbers remain elusive, FeS_2 nanocrystal thin films have been successfully used as the counter electrode for dye sensitized solar cells [10] and as a low-potential barrier back contact to polycrystalline CdS/CdTe thin film solar cells [11].

Detailed understanding of the optical response of FeS_2, in the form of the energy-dependent complex dielectric function, $\varepsilon(E) = \varepsilon_1(E) + i\varepsilon_2(E)$, or alternately the complex refractive index, $N(E) = n(E) + ik(E) = \varepsilon^{1/2}(E)$, spectra is necessary for the continued investigation and future development of PV devices incorporating FeS_2. A limited number of studies have reported on the optical response of iron pyrite employing methods such as optical reflectance [12–14] and spectroscopic ellipsometry measurements [15]. In Choi *et al* [15], analysis is made on the pseudo-dielectric function, $\langle\varepsilon\rangle$, obtained by using a simple model of a discrete interface between a semi-infinite material and known semi-infinite

ambient for a natural single crystal of FeS_2 over the spectral range from 0.5 to 4.5 eV. The measurements in that study, however, are performed at 77 K and did not include optical properties of FeS_2 at room temperature. The absorption coefficient ($\alpha = 4\pi k/\lambda$) of single crystal FeS_2 is presented in Ennaoui *et al* [5] from 0.8 to 2.0 eV. While optical properties of bulk single crystal FeS_2 have been reported, the optical constants of nanocrystalline FeS_2 have not yet been well studied. This work reports comparison of the room temperature optical response obtained by *ex situ* spectroscopic ellipsometry measurements of nanocrystalline thin film and bulk single crystal FeS_2 over the spectral range from 0.735 to 5.887 eV, spanning the near infrared to ultraviolet. Analysis of ellipsometric measurements yields spectra in ε for each

sample, from which critical point electronic transitions are identified.

2. Experimental methods

FeS_2 exists in either pyrite or marcasite crystal structure, both of which share the FeS_2 stoichiometry. Here, we focus on nanocrystal pyrite FeS_2 synthesized using a hot solution injection method in an inert atmosphere. In a Schlenk line system, a mixture of Fe precursor ($FeBr_2$), solvent (oleylamine), and surfactant (trioctylphosphine oxide, TOPO) is heated at 170 °C in a nitrogen environment in a three-neck flask. The sulfur precursor solution (elemental sulfur and oleylamine) is injected into the Fe precursor solution for FeS_2 nanocrystal nucleation. Growth of the nanocrystals takes place at a temperature of 220 °C and standard atmospheric pressure. These nanocrystals consist of highly-pure pyrite phase verified by x-ray diffraction and can be synthesized over sizes ranging from approximately 50 to 150 nm edge lengths [16]. A FeS_2 nanocrystal film was deposited on soda lime glass by solution drop-casting in a layer-by-layer process. During deposition of the nanocrystal thin film, hydrazine treatment at ambient temperature and pressure is used to remove the TOPO, organic hydrocarbon molecules of an insulating nature, from the surface of the nanocrystals to ultimately make the films more conductive. Scanning electron micrographs (SEMs) of FeS_2 nanocrystal films are taken using a Hitachi S-4800 to see the surface morphology of film and the shape and size of the nanocrystals. The pyrite FeS_2 natural bulk single crystal for comparison to the films is sourced from Navajún, La Rioja, Spain. No surface cleaning of the bulk crystal sample is performed prior to the measurement. Room temperature ellipsometric spectra (in $N = \cos 2\Psi$, $C = \sin 2\Psi \cos \Delta$, $S = \sin 2\Psi \sin \Delta$) are collected *ex situ* at 70° angle of incidence using a single rotating

compensator multichannel ellipsometer [17, 18] collecting 696 data points over a spectral range from 0.735 to 5.887 eV (M-2000FI, J A Woollam Co.).

Ellipsometric spectra collected from the nanocrystalline film are analyzed using a structural model that consisted of a semi-infinite glass substrate/FeS_2 nanocrystal thin film/surface roughness/air ambient. The bulk crystal sample is modeled using a semi-infinite bulk FeS_2 layer/surface roughness/air ambient structure. Spectra in ε and the structural parameters, the surface roughness thicknesses and nanocrystal film layer thickness, are extracted by fitting the optical and structural model to the respective experimental ellipsometric spectra. The fitting uses a least square regression analysis that minimized an unweighted error function σ [19]

$$\sigma = \sqrt{\frac{1}{3N - M}\sum_{j=1}^{N}\begin{bmatrix}(\cos 2\Psi_j^{\mathrm{mod}} - \cos 2\Psi_j^{\mathrm{exp}})^2 \\ + (\sin 2\Psi_j^{\mathrm{mod}} \cos \Delta_j^{\mathrm{mod}} - \sin 2\Psi_j^{\mathrm{exp}} \cos \Delta_j^{\mathrm{exp}})^2 \\ + (\sin 2\Psi_j^{\mathrm{mod}} \sin \Delta_j^{\mathrm{mod}} - \sin 2\Psi_j^{\mathrm{exp}} \sin \Delta_j^{\mathrm{exp}})^2\end{bmatrix}}, \quad (1)$$

where N is the number of measured values and M is the number of fit parameters, 'exp' denotes experimental spectra, and 'mod' denotes values generated from the model.

Spectra in ε_2 for nanocrystal film and bulk crystal FeS_2 are modeled using a parametric expression assuming critical points with parabolic bands (CPPB) [20, 21]. Excitonic transitions ($\mu = 1$) are assumed based on Choi *et al* [15]. Kramers–Kronig integration of ε_2 along with a Sellmeier expression [22] and a constant additive term, ε_∞, are used to describe ε_1. The expression for parametrization of ε is

$$\varepsilon_2(E) = \mathrm{Im}\sum_n \frac{A_n \Gamma_n e^{i\varphi_n}}{2E_n - 2E - i\Gamma_n}$$

$$\varepsilon_1(E) = \varepsilon_\infty + \frac{2}{\pi}\frac{AE_0}{(E_0^2 - E^2)}$$

$$+ \frac{2}{\pi}P\int_{0.735}^{5.887}\frac{\xi\varepsilon_2(\xi)}{\xi^2 - E^2}d\xi, \quad (2)$$

where A is the amplitude of the Sellmeier expression and E_0 is the resonance energy which must be outside the measured spectral range. For each CPPB oscillator, A_n is the amplitude, Γ_n is the broadening, E_n is the critical point energy, and ϕ_n is the phase projection factor. Spectra in ε describing the surface roughness of both the nanocrystalline film and bulk crystal FeS_2 are modeled using the Bruggeman effective medium approximation [23, 24]. As both samples are measured *ex situ*, after exposure to atmosphere and without further surface preparation, the surface roughness layer optical response may also be affected by any atmospheric contaminants on the surface. Contributions from physical FeS_2 protrusions and any contaminants on the surface are not separated when modeling the optical response of the surface roughness using Bruggeman effective medium approximation here. When the void fraction in the surface roughness layer and surface roughness thickness are varied, the errors on both exceed the fit value for the thin film. In the case of the bulk
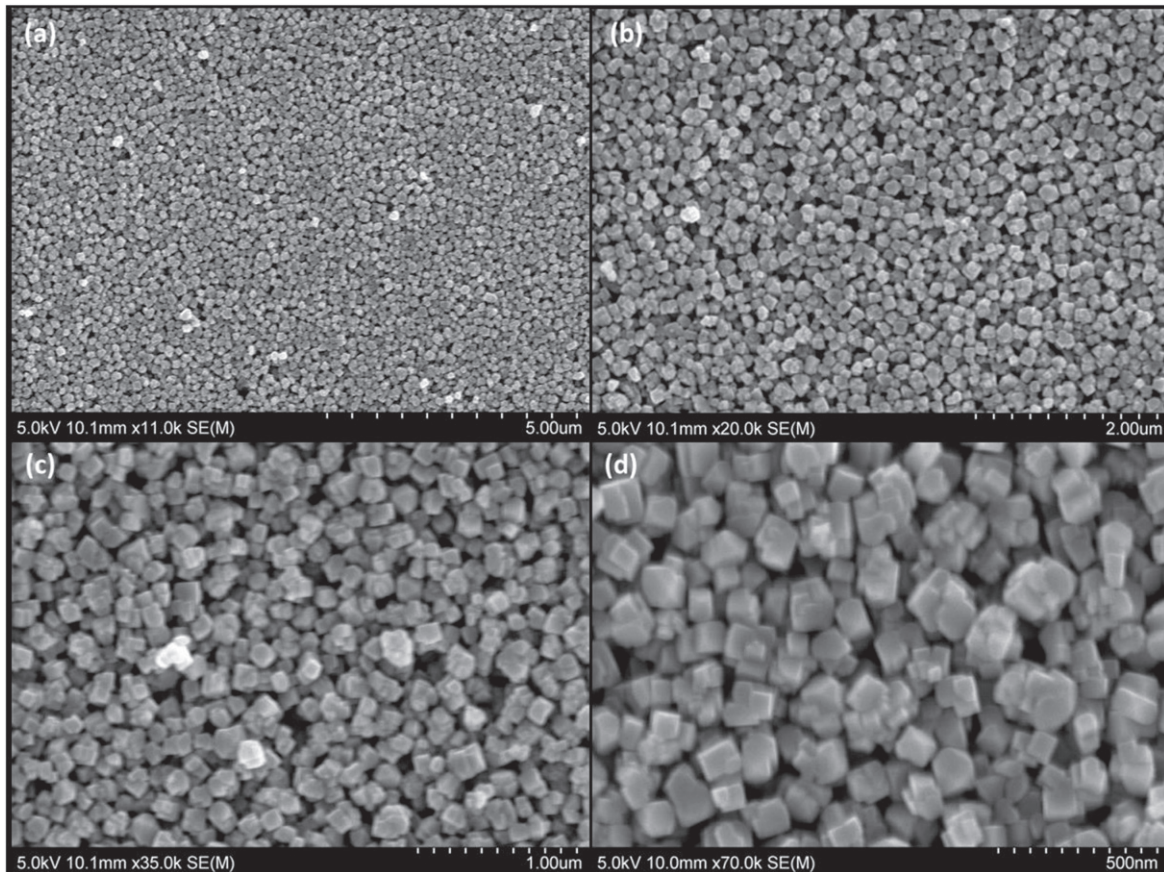
Figure 1. Scanning electron micrographs (SEMs) of FeS$_2$ nanocrystals at four different resolutions.

crystal, void fraction in the surface roughness fit to 0.71 ± 0.07 and surface roughness thickness fit to 8.7 ± 1.0 nm. When the void fraction is fixed at 0.5 for the bulk crystal, a very similar surface roughness thickness of 8.6 ± 0.1 nm is obtained. Therefore, for simplicity and in keeping with Fujiwara *et al* [25], we have fixed the void and FeS$_2$ volume fractions of each at 0.5.

3. Results and discussion

Figure 1 shows SEMs of a nanocrystal film at four different magnifications. The size of each nanocrystal is on average 70–80 nm. From the SEMs, we see that the film is not densely packed and the surface reduces the intensity of light reaching the detector for spectroscopic ellipsometry measurements. As spectroscopic ellipsometry is based on ratios of intensities and electric field amplitudes, as opposed to the absolute values, this scattering is not a limitation of the measurement provided that at least some light reaches the detector.

Figure 2 compares experimental ellipsometric spectra and the model fit for bulk crystal FeS$_2$ and the FeS$_2$ nanocrystal film, and the parameters describing ε for each are given in tables 1 and 2. The values of ε_∞ are 2.86 ± 0.03 for bulk crystal sample and 1.18 ± 0.04 for nanocrystal film. The surface roughness and bulk layer thickness of the nanocrystal thin film sample are 5.8 ± 0.2 and 1854 ± 1 nm,

respectively, with $\sigma = 2.8 \times 10^{-3}$. The surface roughness of the bulk crystal sample is 8.6 ± 0.1 nm with $\sigma = 1.4 \times 10^{-3}$. In both cases, low values of σ indicate that our model is appropriate and calculated parameters are reliable. These thickness values are from the parametric fit of ellipsometric spectra collected at a single position on the sample surface and, since the nanocrystalline film is expected to exhibit significant non-uniformity, are not considered as an average of film thickness across the entire sample.

After obtaining the thicknesses from the parametric models, numerical inversion [26] is used to extract ε at each spectral point for the two samples over the full measured spectral range. Figures 3 and 4 show numerically inverted spectra in ε for the bulk crystal and nanocrystalline film. Spectra in α are obtained from the numerically inverted values of ε and are compared in figure 5. The seven critical points observed here in ε for the bulk crystal material are in agreement with Choi *et al* [15], while only four critical points are resolved for the nanocrystal film. The large feature in the complex dielectric function spectra near 2.0 eV is due to transitions between Fe atom electron orbitals. The origin of large feature near 3.5 eV is a mixture of Fe 3d and S 3p orbitals. The detailed physics behind the origin of these features are described in Choi *et al* [15].

The amplitudes of the features in ε of the nanocrystal film are smaller in magnitude when compared to those of the bulk single crystal. Features at some critical point energies appear
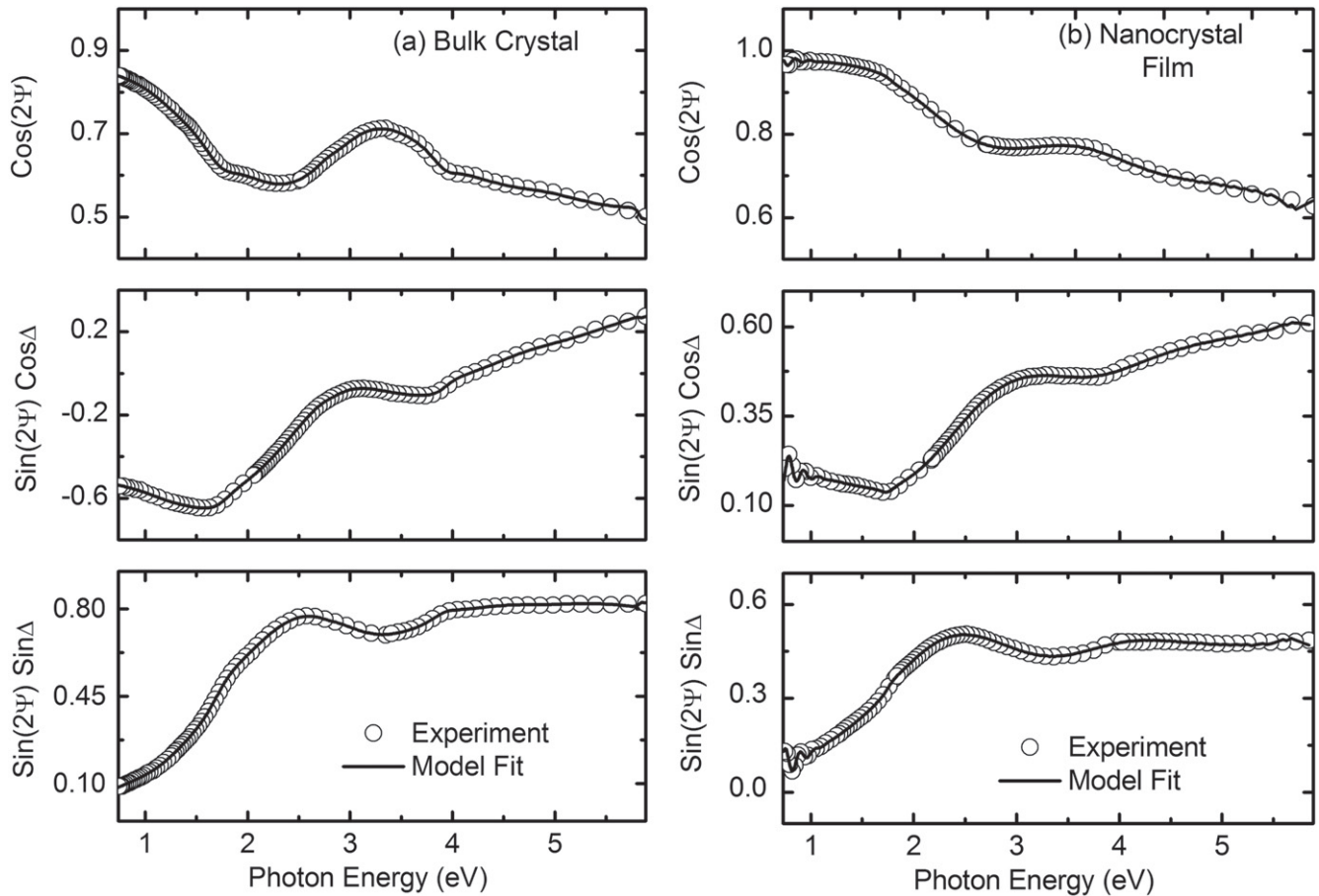
Figure 2. Experimental ellipsometric spectra (open circles) and model fit (solid lines) of (a) bulk, single-crystal FeS$_2$ pyrite and (b) a nanocrystalline pyrite FeS$_2$ thin film over the spectral range from 0.735 to 5.887 eV. The data point density shown is reduced for clarity.

to diminish due to lower transition strength and higher critical point broadening, making them more difficult to resolve in general. For the film, we are not able to resolve the critical point at 1.16 eV possibly due to the presence of defects [9], which gives rise to noticeable sub-bandgap absorption near this critical point, or simply a lack of sensitivity as that feature is relatively low in amplitude. Features near 1.7 and 2.0 eV are observed in both the nanocrystal film and bulk crystal. The critical point at 2.78 eV for bulk single crystal has relatively low amplitude, 0.46, which is further reduced in the nanocrystal film and below the sensitivity of our analysis. The two features observed at 3.65 and 3.90 eV for the single crystal cannot be individually resolved in the case of the nanocrystalline film due to enhanced scattering and low amplitude and are therefore represented by a single feature at 3.78 eV. Additional features at 4.87 and 5.3 eV are observed for both the bulk crystal and nanocrystalline film respectively. To address this issue, the optical response of the crystal component of the film is extracted. Two features at 3.65 and 3.90 eV are resolved, although the others at 2.78 and 1.16 eV are still not accessible.

The indirect band gap of bulk single crystal FeS$_2$ is reported to be 0.95 eV [5, 27], and the band gap of a FeS$_2$ nanocrystalline film is reported at 1.10 eV [28]. Both samples in this study show significant absorption below the reported

value of band gap, as can be seen in both α and ε_2. This behavior has been attributed to large amounts of random defects interacting with the conduction band, or a disordered structure that can create an Urbach tail near the absorption onset [29]. This behavior may be due to presence of a native oxide, complex roughness, and hydrocarbon contamination on the surfaces [30]. Spectra in ε of bulk single crystal FeS$_2$ are in close qualitative agreement with that collected for a pyrite crystal at 77 K [15]. In comparison, the nanocrystalline FeS$_2$ film clearly shows enhanced optical absorption below the lowest energy critical point, indicating higher density of sub-band gap electronic states originating from defects either in the crystallites, their surfaces, or in both [9, 11, 16].

The difference in the size of ordered regions between the bulk crystal and nanocrystal samples can result in different surface energy interactions and interface energy. These variations are reflected in ε and α for nanocrystalline and bulk FeS$_2$ as shown in figures 3 and 5. Due to high values of α, this material is a good candidate for the absorber in PV technologies, although poor electronic quality has thus far limited its application. Spectra in α of the hydrazine treated FeS$_2$ nanocrystal film obtained by spectroscopic ellipsometry here agrees reasonably well with that measured from 0.62 to 4.13 eV for a non-hydrazine treated FeS$_2$ nanocrystal film made by the same method [16]. Absorption data for a bulk single crystal FeS$_2$ [5]

5

Table 1. Parameters describing spectra in ε for bulk crystal FeS$_2$ at room temperature. Critical point energies measured at $T = 77$ K reported by Choi *et al* [15] are also provided for comparison.

CP (n)	1	2	3	4	5	6	7	Sellmeier
Critical point energy (eV) [15]	1.36	1.78	2.09	2.49	3.41	3.92		
E_n (eV)	1.16 ± 0.04	1.72 ± 0.01	1.99 ± 0.02	2.78 ± 0.03	3.65 ± 0.05	3.90 ± 0.01	4.87 ± 0.07	6.23 ± 0.01
A_n	2.3 ± 0.4	14.5 ± 0.8	27 ± 1	0.46 ± 0.09	11.3 ± 0.3	2.0 ± 0.1	1.0 ± 0.3	6.9 ± 0.1 eV
Γ_n (eV)	0.66 ± 0.06	0.40 ± 0.01	1.17 ± 0.03	0.30 ± 0.06	2.0 ± 0.1	0.35 ± 0.02	1.0 ± 0.2	
ϕ_n (°)	−173 ± 21	−16 ± 5	−9 ± 4	−80 ± 19	−45 ± 6	59 ± 8	−94 ± 16	

Table 2. Parameters describing spectra in ε for the FeS$_2$ nanocrystal thin film at room temperature.

CP (n)	1	2	3	4	Sellmeier
E_n(eV)	1.75 ± 0.01	2.05 ± 0.01	3.78 ± 0.05	5.3 ± 0.6	7.6 ± 0.1
A_n	0.20 ± 0.01	3.3 ± 0.1	0.9 ± 0.2	1.3 ± 0.2	10.1 ± 0.6 eV
Γ_n (eV)	0.20 ± 0.02	1.60 ± 0.03	1.6 ± 0.1	6 ± 2	
ϕ_n (°)	-54 ± 8	-11 ± 2	-30 ± 10	-28 ± 17	
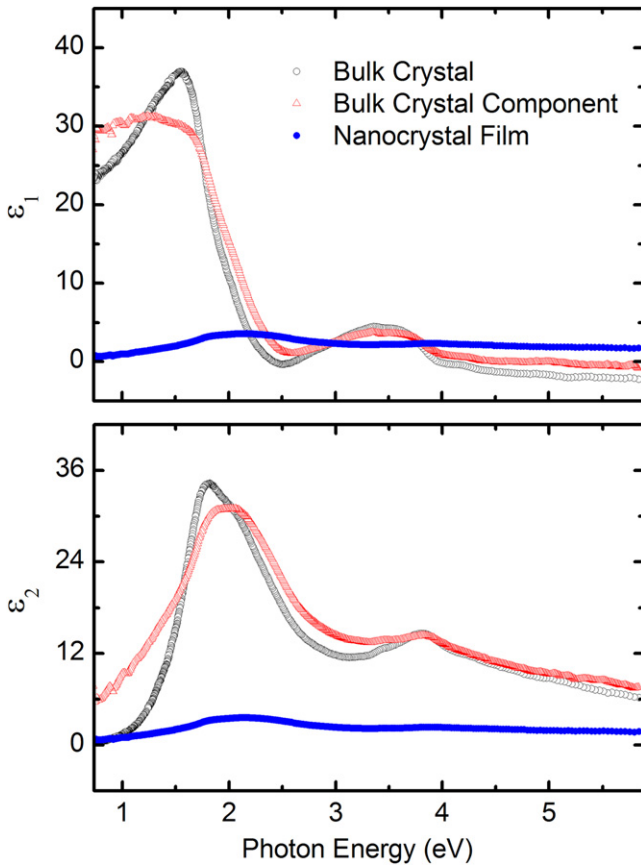
Figure 3. Complex dielectric function, $\varepsilon = \varepsilon_1 + i\varepsilon_2$, spectra for the bulk crystal (black open circle) and nanocrystal film (blue solid circle) FeS$_2$ obtained from numerical inversion. Spectra in ε are also shown for the bulk crystal component within the thin film (red triangle).

is in qualitative agreement with α in figure 5 from 0.8 to 2.0 eV. In both cases the results in figure 5 have slightly higher values of α near the first critical point and some small features in the higher energy range corresponding to critical point transitions. In comparison, α from [5] and [16] are rather flat at higher energies where the sample is likely optically opaque. In that regime, polarization based reflectance measurements like spectroscopic ellipsometry provide better sensitivity compared to unpolarized intensity based reflectance. Ellipsometry is less sensitive in the region where the material is weakly absorbing, with smaller values of α, like any reflection based technique [31, 32]. In the cases of both samples, α is large in the vicinity of the reported band gap.

Although the bulk single crystal has fewer surfaces and interfaces, the mean size of ordered regions within samples impact ε and α implying that both samples are likely not well ordered. The nanocrystals are geometrically smaller; however the bulk crystal sample could still possess a large concentration of impurities limiting the size of ordered regions and reducing the mean scattering time of charge carriers. Increases in impurities and interfacial area, due to both free surfaces and grain boundaries, will increase broadening of critical point features and enhance the magnitude of Urbach tails and absorption below the band gap.

The optical and electrical properties, such as increasing the band gap energy, can be altered in FeS$_2$ by tuning the crystal sizes [33]. Although quantum confinement effects are not expected for the nanocrystal sizes utilized here, we observed a small blue shift in features in ε and critical point energies near 1.7 and 2.0 eV when comparing the nanocrystal film with the single crystal bulk. There are several reasons for this blue shift. At dimensions larger than the Bohr excitonic radius, the confinement of the electron–hole pair is very weak and size-dependent changes in energy levels are relatively smaller [34]. To further model the FeS$_2$ material component in the nanocrystalline film, a Bruggeman effective medium approximation consisting of ε for bulk crystal FeS$_2$ and void is fit to ε already determined for nanocrystalline film. The best fit using this approach has 0.380 ± 0.001 volume fraction occupied by bulk crystal material. Then, using this structural result the optical properties of the FeS$_2$ material component are re-calculated using numerical inversion and, finally, that inverted result is re-parametrized by using the excitonic CPPB model described earlier. Numerically inverted ε of the FeS$_2$ component in the nanocrystal thin film are shown in figure 3 for comparison. The parameters describing this new ε of the FeS$_2$ material itself are shown in table 3. The value of ε_∞ is 3.38 ± 0.05 with $\sigma = 3.4 \times 10^{-3}$.

As can be seen in table 3, a blue shift occurs in the two lowest energy detectable critical points of the bulk crystal fraction of FeS$_2$ in the nanocrystalline film as compared with the critical point energies seen in the bulk sample only. For films comprised of small nanocrystallites, such as those seen in figure 1, this kind of effect is significant [35]. Because of the high surface-to-volume ratio in the nanocrystal film, surface defects, such as vacancies and dangling bonds, are commonly observed in addition to defects already present within the bulk of each crystallite [36]. Nanocrystal size can be controlled by the amount of surfactant added during synthesis, yielding 50–150 nm crystallites. The average nanocrystallites in this film are approximately 70–80 nm in size. The blue shift in critical point features for nanocrystal film may also be due to increased oxidation of films when exposed to air in comparison to bulk crystal FeS$_2$. Density
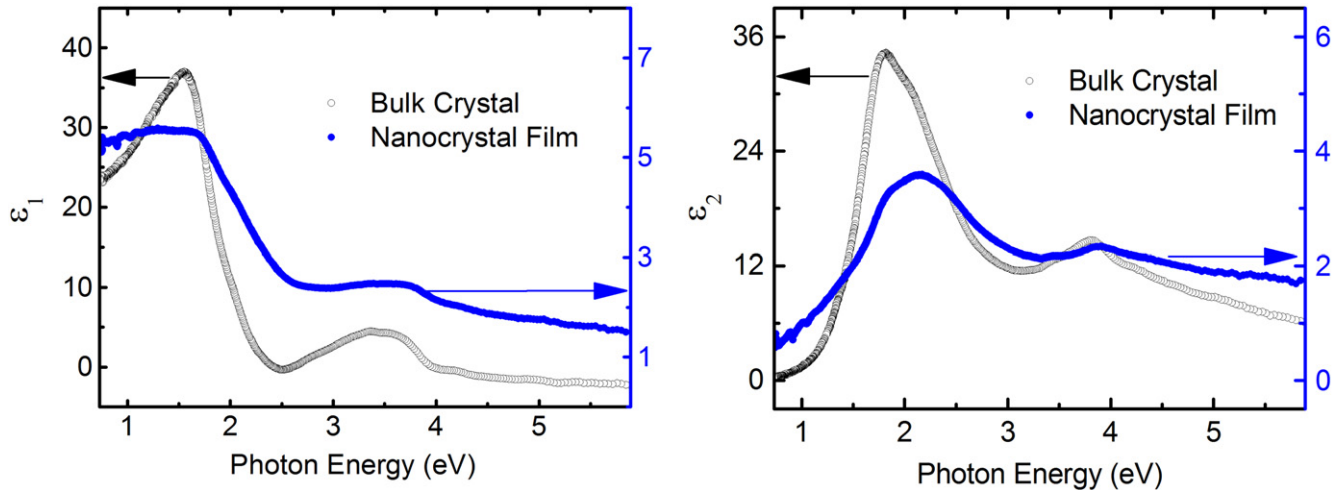
Figure 4. Rescaled spectra of ε, highlighting qualitative difference in the line shape of bulk crystal (black open circle) and nanocrystal FeS$_2$ (blue solid circle).
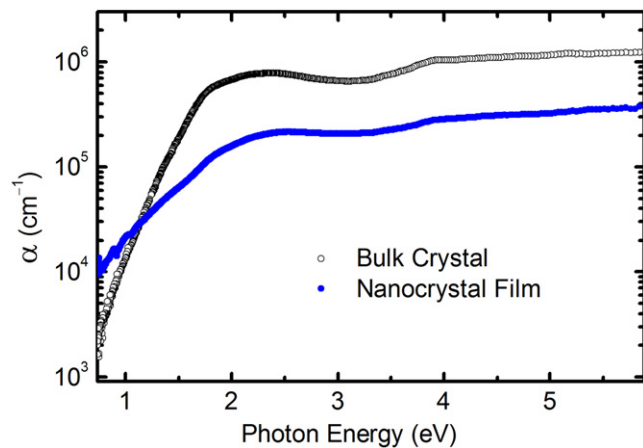
Figure 5. Absorption coefficient (α) obtained from numerical inverted ε for bulk crystal (black open circles) and nanocrystal film (blue solid circles) FeS$_2$.

functional theory studies have reported a 0.2–0.3 eV band gap increase is possible when 10% of the sulfur is replaced with oxygen [37]. This band gap increase may arise due to the synthesis process or the capping reagent, which impacts the growth of the nanocrystals. Another possibility involves Burstein–Moss effect where the absorption edge is blue shifted to higher energies when conduction band states are occupied [38].

Scattering of charge carriers mainly depends on the amount of grain boundaries resulting from the small grain size. Lifetime of charge carriers decreases due to this scattering and causes broadening of critical points [39]. We observe significant reduction of the amplitude and increase in broadening of all the oscillators used to model the nanocrystalline film when compared to the bulk crystal with the exception of the features at 1.75 eV. The reduction of amplitude of features in ε is an effect of nanocrystals, resulting in a change of oscillator strengths that are associated with the optical transitions.

Impurities may also exist within these nanocrystal grains. Seefeld *et al* [14] studied impurity concentration in FeS$_2$ films fabricated by solution phase deposition method using Auger electron spectroscopy (AES) and secondary ion mass spectroscopy (SIMS) depth profiles. AES measurements detect large amount of K and smaller amount of Na, O, and C for the film deposited on Mo-coated glass and Mo-coated crystal Si substrates. Similarly, SIMS profiles show the concentration of C, H, O, Na, K, Al, Ca, and Mg as a function of depth into the film stack. In [14], the largest impurity concentration is 0.9 atom% oxygen. Similarly, x-ray photoelectron spectroscopy conducted for FeS$_2$ films deposited on different substrates showed impurities of O, C, K, and Na in [14] which are potentially from the substrates, precursor compound, and oxygen when the film is annealed in air. Berry *et al* [40] studied pyrite FeS$_2$ films fabricated by atmospheric-pressure chemical vapor deposition (CVD). Similar experimental research on CVD deposited films showed lower impurity concentration than solution deposited FeS$_2$ films annealed in an argon atmosphere. Limpinsel *et al* [41] reported on efforts to prepare highly pure single crystal FeS$_2$, and found that while O, C, and N are present, the crystals also show Si, B, Na, and Cr impurities.

Impurities in the nanocrystals here likely arise principally from the source materials. For example, the purity of iron precursor FeBr$_2$ is only 98%, elemental sulfur is 99.99%, TOPO is 99%, and oleylamine is only 80%–90%. FeS$_2$ nanocrystal synthesis is conducted in a nitrogen environment using Schlenk lines and film fabrication is also in a nitrogen atmosphere. Structural and compositional properties of FeS$_2$ nanocrystal thin films fabricated in this system have been investigated using x-ray diffraction, Raman spectroscopy and scanning electron microscopy as previously published [16]. The FeS$_2$ nanocrystals are found to be phase pure with no evidence of other crystal structures. Since nanocrystal film fabrication is conducted in a nitrogen environment glove box, the nanocrystal films are only exposed to air for a short duration of time for spectroscopic ellipsometry data

Table 3. Parameters describing spectra in ε for the FeS$_2$ component fraction of the nanocrystal film.

CP (n)	1	2	3	4	5	Sellmeier
Bulk crystal	1.72 ± 0.01	1.99 ± 0.02	3.65 ± 0.05	3.90 ± 0.01	4.87 ± 0.07	
E_n (eV)	1.83 ± 0.02	2.06 ± 0.01	3.5 ± 0.1	3.89 ± 0.02	4.67 ± 0.06	6.49 ± 0.02
A_n	2.5 ± 0.2	30.2 ± 0.3	13.5 ± 0.3	1.3 ± 0.1	1.80 ± 0.02	11.8 ± 0.4 eV
Γ_n (eV)	0.20 ± 0.03	1.30 ± 0.02	3.3 ± 0.1	0.35 ± 0.03	1.10 ± 0.16	
ϕ_n (°)	25 ± 12	8 ± 2	-43 ± 4	37 ± 9	180 ± 16	

collection. Additionally, application of these nanocrystal films as back contacts to CdTe solar cells [11] shows stability in air for up to several weeks. Therefore we expect any dynamic roles of oxygen in the samples to be minimal.

4. Conclusions

Optical properties for bulk crystal and nanocrystal thin film FeS$_2$ have been determined over a spectral range from 0.735 to 5.887 eV by spectroscopic ellipsometry. Spectra in ε for the bulk crystal shows seven interband critical points while the nanocrystal film shows only four. Small blue shifting of critical point energies are observed in the nanocrystal film compared to the bulk material for corresponding transitions. The number of transitions observed is reduced in the nanocrystal film due to a combination of increased scattering and decreased transition strength. FeS$_2$ has some characteristics suitable for PV, including high optical absorption. Further study of variations in ε as a function of various processing conditions for films would likely be useful in optically identifying structural and electronic property variations.

Acknowledgments

References

[1] Bragg W L 1913 The structure of some crystals as indicated by their diffraction of x-rays *Proc. R. Soc.* A **89** 248–77
[2] Bullett D W 1982 Electronic structure of 3d pyrite- and marcasite-type sulphides *J. Phys. C: Solid State Phys.* **15** 6163
[3] Sithole H, Ngoepe P and Wright K 2003 Atomistic simulation of the structure and elastic properties of pyrite (FeS$_2$) as a function of pressure *Phys. Chem. Miner.* **30** 615–9
[4] Ennaoui A and Tributsch H 1984 Iron sulphide solar cells *Sol. Cells* **13** 197–200
[5] Ennaoui A, Fiechter S, Pettenkofer C, Alonso-Vante N, Büker K, Bronold M, Höpfner C and Tributsch H 1993 Iron disulfide for solar energy conversion *Sol. Energy Mater. Sol. Cells* **29** 289–370
[6] Altermatt P P, Kiesewetter T, Ellmer K and Tributsch H 2002 Specifying targets of future research in photovoltaic devices containing pyrite (FeS$_2$) by numerical modelling *Sol. Energy Mater. Sol. Cells* **71** 181–95
[7] Wadia C, Wu Y, Gul S, Volkman S K, Guo J and Alivisatos A P 2009 Surfactant-assisted hydrothermal synthesis of single phase pyrite FeS$_2$ nanocrystals *Chem. Mater.* **21** 2568–70
[8] Puthussery J, Seefeld S, Berry N, Gibbs M and Law M 2010 Colloidal iron pyrite (FeS$_2$) nanocrystal inks for thin-film photovoltaics *J. Am. Chem. Soc.* **133** 716–9
[9] Bi Y, Yuan Y, Exstrom C L, Darveau S A and Huang J 2011 Air stable, photosensitive, phase pure iron pyrite nanocrystal thin films for photovoltaic application *Nano Lett.* **11** 4953–7
[10] Shukla S *et al* 2014 Iron pyrite thin film counter electrodes for dye-sensitized solar cells: high efficiency for iodine and cobalt redox electrolyte cells *ACS Nano* **8** 10597–605
[11] Bhandari K P, Koirala P, Paudel N R, Khanal R R, Phillips A B, Yan Y, Collins R W, Heben M J and Ellingson R J 2015 Iron pyrite nanocrystal film serves as a copper-free back contact for polycrystalline CdTe thin film solar cells *Sol. Energy Mater. Sol. Cells* **140** 108–14
[12] Bither T A, Bouchard R, Cloud W, Donohue P and Siemons W 1968 Transition metal pyrite dichalcogenides. High-pressure synthesis and correlation of properties *Inorg. Chem.* **7** 2208–20
[13] Schlegel A and Wachter P 1976 Optical properties, phonons and electronic structure of iron pyrite (FeS$_2$) *J. Phys. C: Solid State Phys.* **9** 3363–9
[14] Seefeld S, Limpinsel M, Liu Y, Farhi N, Weber A, Zhang Y, Berry N, Kwon Y J, Perkins C L and Hemminger J C 2013 Iron pyrite thin films synthesized from an Fe(acac)3 ink *J. Am. Chem. Soc.* **135** 4412–24
[15] Choi S G, Hu J, Abdallah L S, Limpinsel M, Zhang Y N, Zollner S, Wu R Q and Law M 2012 Pseudodielectric function and critical-point energies of iron pyrite *Phys. Rev.* B **86** 115207
[16] Bhandari K P, Roland P J, Kinner T, Cao Y, Choi H, Jeong S and Ellingson R J 2015 Analysis and characterization of iron pyrite nanocrystals and nanocrystalline thin films derived from bromide anion synthesis *J. Mater. Chem.* A **3** 6853–61
[17] Lee J, Rovira P, An I and Collins R 1998 Rotating-compensator multichannel ellipsometry: applications for real time Stokes vector spectroscopy of thin film growth *Rev. Sci. Instrum.* **69** 1800–10
[18] Johs B D, Woollam J A, Herzinger C M, Hilfiker J N, Synowicki R A and Bungay C L 1999 Overview of variable-angle spectroscopic ellipsometry (VASE): II. Advanced applications *Opt. Meterology* CR **72** 29–58
[19] Johs B and Herzinger C M 2008 Quantifying the accuracy of ellipsometer systems *Phys. Status Solidi* c **5** 1031–5
[20] Cardona M 1969 *Modulation Spectroscopy Suppl. 11 of Solid State Physics* ed F Seitz *et al* (New York: Academic) pp 15–25
[21] Aspnes D E 1980 *Handbook on Semiconductors* vol 2 ed M Balkanski (Amsterdam: North-Holland) pp 125–7

[22] Collins R W and Ferluto A S 2005 *Handbook of Ellipsometry* ed H Tompkins and E Irene (Norwich, NY: William Andrew) pp 93–233

[23] Bruggeman D A G 1935 Berechnung verschiedener physikalischer konstanten von heterogenen substanzen: I. Dielektrizitätskonstanten und leitfähigkeiten der mischkörper aus isotropen substanzen *Ann. Phys.* **416** 636–64

[24] Aspnes D, Theeten J and Hottier F 1979 Investigation of effective-medium models of microscopic surface roughness by spectroscopic ellipsometry *Phys. Rev.* B **20** 3292–302

[25] Fujiwara H, Koh J, Rovira P I and Collins R W 2000 Assessment of effective-medium theories in the analysis of nucleation and microscopic surface roughness evolution for semiconductor thin films *Phys. Rev.* B **61** 10832

[26] Oldham W G 1969 Numerical techniques for the analysis of lossy films *Surf. Sci.* **16** 97–103

[27] Ferrer I, Nevskaia D, De las Heras C and Sanchez C 1990 About the band gap nature of FeS_2 as determined from optical and photoelectrochemical measurements *Solid State Commun.* **74** 913–6

[28] Lucas J M, Tuan C-C, Lounis S D, Britt D K, Qiao R, Yang W, Lanzara A and Alivisatos A P 2013 Ligand-controlled colloidal synthesis and electronic structure characterization of cubic iron pyrite (FeS_2) nanocrystals *Chem. Mater.* **25** 1615–20

[29] Lazić P, Armiento R, Herbert F, Chakraborty R, Sun R, Chan M, Hartman K, Buonassisi T, Yildiz B and Ceder G 2013 Low intensity conduction states in FeS_2: implications for absorption, open-circuit voltage and surface recombination *J. Phys.: Condens. Matter* **25** 465801

[30] Aspnes D E and Studna A A 1981 Chemical etching and cleaning procedures for Si, Ge, and some III-V compound semiconductors *Appl. Phys. Lett.* **39** 316–8

[31] Ghimire K, Haneef H F, Collins R W and Podraza N J 2015 Optical properties of single-crystal $Gd_3Ga_5O_{12}$ from the infrared to ultraviolet *Phys. Status Solidi* b **252** 2191–8

[32] Fujiwara H 2007 *Spectroscopic Ellipsometry: Principles and Applications* (New York: Wiley) pp 137–9

[33] Li W, Döblinger M, Vaneski A, Rogach A L, Jäckel F and Feldmann J 2011 Pyrite nanocrystals: shape-controlled synthesis and tunable optical properties via reversible self-assembly *J. Mater. Chem.* **21** 17946–52

[34] Efros A L and Rosen M 2000 The electronic structure of semiconductor nanocrystals 1 *Annu. Rev. Mater. Sci.* **30** 475–521

[35] Ahmed F, Naciri A E and Grob J 2010 Optical properties of embedded ZnTe nanocrystals in SiO_2 thin layer *Phys. Status Solidi* a **207** 1619–22

[36] Burda C, Chen X, Narayanan R and El-Sayed M A 2005 Chemistry and properties of nanocrystals of different shapes *Chem. Rev.* **105** 1025–102

[37] Hu J, Zhang Y, Law M and Wu R 2012 Increasing the band gap of iron pyrite by alloying with oxygen *J. Am. Chem. Soc.* **134** 13216–9

[38] Layek A, Middya S and Ray P P 2013 Increase in open circuit voltage by the incorporation of band gap engineered FeS_2 nanoparticle within MEHPPV solar cell *J. Mater. Sci., Mater. Electron.* **24** 3749–55

[39] Agocs E, Nassiopoulou A G, Milita S and Petrik P 2013 Model dielectric function analysis of the critical point features of silicon nanocrystal films in a broad parameter range *Thin Solid Films* **541** 83–6

[40] Berry N, Cheng M, Perkins C L, Limpinsel M, Hemminger J C and Law M 2012 Atmospheric-pressure chemical vapor deposition of iron pyrite thin films *Adv. Energy Mater.* **2** 1124–35

[41] Limpinsel M, Farhi N, Berry N, Lindemuth J, Perkins C L, Lin Q and Law M 2014 An inversion layer at the surface of n-type iron pyrite *Energy Environ. Sci.* **7** 1974–89